Combustion instability mitigation by magnetic fields

Agnes Jocher* and Heinz Pitsch
RWTH Aachen University, Institute for Combustion Technology, 52056 Aachen, Germany

Thomas Gomez
Université de Lille I, 59655 Villeneuve d'Ascq, France

Jérôme Bonnety and Guillaume Legros†
Sorbonne Universités, UPMC Univ Paris 06, CNRS, UMR 7190 Institut Jean le Rond d'Alembert, 75005 Paris, France
(Received 15 August 2016; revised manuscript received 12 April 2017; published 22 June 2017)

The present interdisciplinary study combines electromagnetics and combustion to unveil an original and basic experiment displaying a spontaneous flame instability that is mitigated as the non-premixed sooting flame experiences a magnetic perturbation. This magnetic instability mitigation is reproduced by direct numerical simulations to be further elucidated by a flow stability analysis. A key role in the stabilization process is attributed to the momentum and thermochemistry coupling that the magnetic force, acting mainly on paramagnetic oxygen, contributes to sustain. The spatial local stability analysis based on the numerical simulations shows that the magnetic field tends to reduce the growth rates of small flame perturbations.

DOI: 10.1103/PhysRevE.95.063113

I. INTRODUCTION

Spontaneous low-frequency oscillations of atmospheric non-premixed coflow flames were found to be induced by buoyancy-driven Kelvin-Helmholtz (KH) instabilities [1]. These instabilities can be triggered by a shear layer in a flow and might appear in the atmosphere, oceans, and stellar internal flows [2]. The prediction and the subsequent control of stability limits is of significant interest not only in flames and nature but also in a wide range of industrial applications [3], for example, the oxyfuel combustion technique [4]. This technique reduces anthropogenic CO_2 release into the atmosphere due to high O_2 concentrations and recycled combustion products—mainly water vapor and CO_2—in the unburnt oxidizing stream. Doing so, the peak soot content generated along the combustion process is also decreased. A major drawback of the technology is the enhanced tendency to combustion instability, especially caused by CO_2 addition. This leads to limited combustion reliability and in the worst case to mechanical failure and damage of the whole system. Furthermore, in unstable combustion regimes, the likelihood of unburnt fuel and soot expulsion increases due to local flame quenching and suppressed oxidation processes. The harmful effects of soot particles on human health and the environment have been discussed extensively [5–7] and have led to the tightening of regulations by governments on emission sources like vehicles and power plants as well as on the ambient concentration itself [8–10]. To help overcome these drawbacks, we suggest to combine technologies. Although special attention has been paid to the combustion enhancing role of electric fields [11,12], the stability of flames experiencing magnetic perturbations has not been thoroughly examined. It was shown in the literature that the onset of the KH instabilities in non-premixed flames can be suppressed by increased soot production and the subsequent flame cooling due to the associated enhanced radiative emission by soot particles [13]. An upward gradient of the square of the magnetic flux density $\nabla(\mathbf{B}^2)$ applied to a steady laminar non-premixed sooting coflow flame was shown to enhance soot formation in the flame, while the formed soot was still fully oxidized, i.e., no soot was released through the flame tip [14]. Furthermore, experiments [15] evidenced that buoyancy-induced convection in non-premixed flames can be partly substituted, enhanced, or reduced by magnetic fields. In several patents, significant reductions in NO_x and CO emissions have been documented when permanent magnets were located around the fuel injector of an internal combustion engine [16–18]. However, to our knowledge, no experimental evidence for a non-premixed flame stabilization and soot emission modification has been shown in an academic configuration until now.

Here, we document the experimental observation of stabilizing a spontaneously oscillating non-premixed sooting flame with a magnetic field. The context of oxyfuel combustion technique is addressed. We analyze the observation with the help of numerical simulations, applying the aforementioned magnetic effects on both mass transfer and soot production to reveal an original phenomenology that potentially allows us to control the stability domain of reacting flows, which is then evidenced by a local stability analysis. The new methodology that could be imagined from the results presented here is especially relevant to oxygen-enhanced and carbon dioxide–diluted combustion strategies and therefore to low-impact combustion devices.

II. EXPERIMENTAL OBSERVATIONS AND PROCEDURE

The present study was initiated after we had observed an unexpected response to an external magnetic perturbation of a non-premixed flame that exhibits natural low-frequency (12.6-Hz) flickering. Indeed, this spontaneous instability vanished as the flame was submitted to a magnetic field generated by an electromagnet. The movie provided as

*Also at Sorbonne Universités, UPMC Univ Paris 06, CNRS, UMR 7190 Institut Jean le Rond d'Alembert, 75005 Paris, France.
†guillaume.legros@upmc.fr

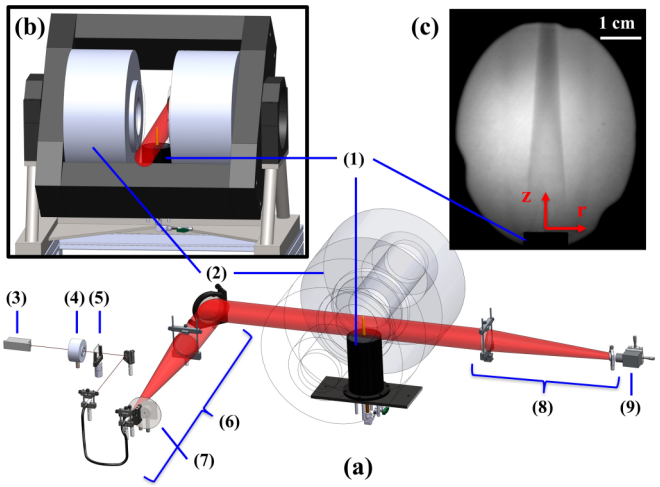

FIG. 1. (a) Schematic of the arrangement allowing the experiment: (1) coflow burner, (2) coils of the electromagnet, (3) continuous wave laser, (4) shutter, (5) neutral density filter, (6) set of beam expanding optics, (7) rotating diffusive disk, (8) set of collection optics, and (9) camera. (b) Close-up view of the laser beam crossing the flame in between both coils. (c) Typical frame captured by the camera as the shutter is open. The burner tip can be seen at the bottom and the soot layer produced in the flame right above.

Supplemental Material [19] displays the time-history of the raw data documenting the initial experiment. The evolution of the non-premixed flame with time is captured by a Phantom v711 high-speed camera equipped with a widescreen complementary metal–oxide–semiconductor (CMOS) sensor. To record this direct visualization of the experiment, the camera just substituted the one shown in Fig. 1(a). A sequence of 48 s at 188 frames per second of 12-bit monochrome frames is captured on an 800×304 pixel^2 matrix. The exposure time was kept constant at 5.3 ms and the camera was focused on the plane containing the flame's vertical axis of symmetry, using a SIGMA 105-mm F2.8 Macro lens. With this optical arrangement, each pixel in the CMOS array focused light from a volume corresponding to 0.13 mm in height, 0.13 mm in width, and 1 mm in depth. The voltage V delivered by a photodiode evidences the magnitude of the flames radiative signature along the experiment. Starting with the spontaneously flickering flame when no magnetic field is applied, the current I flowing through the coils of the electromagnet is gradually increased up to 60 A, generating a maximum magnetic field magnitude of 1 T and a maximum $\nabla(\mathbf{B}^2)$ of 18.2 T^2/m. The voltage evolution delivered by the photodiode evidences that the flame flickering is fully suppressed for the maximum current flowing through the coils of the electromagnet. In the following, experimental, numerical, and theoretical tools are deployed to assess this original stabilization process.

Figure 1(a) displays the setup that enables this experiment together with the associated investigations. As extensively outlined by Jocher *et al.* [14], the burner used (1) is inserted between both coils (2) of the electromagnet, with the burner's exit plane located 130 mm below the coils' horizontal axis of symmetry. Thus, within the volume occupied by the non-premixed flame investigated here, a constant upward $\nabla(\mathbf{B}^2)$ [14] can be generated with a decently uniform maximum magnitude of 18.2 T^2/m. In the following, the case without magnetic field is called MagF0 and the one with $|\nabla(\mathbf{B}^2)| = 18.2$ T^2/m is referred to as MagF1. None of the rig components is magnetic to avoid mechanical interferences. By virtue of its design and size, the whole arrangement cannot be considered a practical combustion device as the experimental flame height does not exceed 5 cm, while the outer diameter of the coils is 80 cm [see Fig. 1(b)]. Practical combustion devices exhibiting the same effect could be designed smaller than the current academic experiment. However, for appropriate modeling and analysis this academic arrangement was chosen to establish well-controlled and spatially constant conditions in terms of $\nabla(\mathbf{B}^2)$.

For the present study, the axisymmetric laminar, flickering, non-premixed ethylene flame shown in the movie burns in 55% oxygen mixed with 45% carbon dioxide in volume, on a Santoro type coflow burner [20]. Ethylene is chosen as a fuel because its sooting propensity is documented in a large body of literature and an extensively studied detailed mechanism including polycyclic aromatic hydrocarbon (PAH) chemistry is available [21,22]. The coflow burner consists of concentric brass tubes with effective inner diameters of $D_f = 11$ mm and $D_{ox} = 102$ mm. The flow rates of the axial ethylene stream and the coflowing oxidizer are adjusted by two Bronkhorst EL-FLOW mass flow controllers to 0.36 l/min and 74 l/min, respectively. The corresponding Reynolds numbers for these conditions are 87 and 1438, respectively. Even though the flow is laminar, the non-premixed flame exhibits spontaneous flickering [23]. It is worth noting that the stabilization process documented hereafter could not be observed for a low sooting, flickering, non-premixed methane flame at similar fluid dynamic conditions.

To track the soot volume fraction distribution, the laser extinction method (LEM) [23,24] is applied, providing two-dimensional soot volume fraction fields with both fine temporal and spatial resolutions. The arrangement of the optical diagnostics to conduct LEM specifically through a flame located in the electromagnet is shown in Figs. 1(a) and 1(b). The system consists of a 100-mW continuous wave laser (3) operating at 645 nm ($-5/+7$ nm) as the monochromatic light source, a neutral density filter (4) to adjust the intensity of the laser, a set of beam expanding optics (6) including a rotating diffusive disk (7) to generate a uniform beam intensity, a set of collection optics (8), and a camera (9). A digital pulse generator controls the occurrence and the duration of the CMOS exposure, together with the shutter (4) opening. A frame grabber records on a computer the frames captured by the camera, such as the one shown in Fig. 1(a). The Photon Focus MV1 12-bit progressive scan monochrome camera (9) is mounted with a conventional lens equipped with a narrow band filter centered at 645 nm (± 2 nm) and whose bandwith at one half the transmissivity maximum is 20 nm. With this optical arrangement, the matrix of 1312×1082 pixels^2 provides a spatial resolution of 137 μm for the LEM projected data over the 60-mm-diameter area of investigation. For the current study, the frames were recorded at a frame rate of 94 Hz and an exposure time of 5.4 ms. The flame is considered an emitting, absorbing, but nonscattering medium. For the laminar coflow non-premixed ethylene flames studied, the flame radiative spectrum in the

visible is governed by the continuum radiation from soot. This is particularly true in the upper part of the visible spectrum. In addition, absorption by soot particles produced in these non-premixed flames is shown to be at least one order of magnitude higher than scattering, especially at large wavelengths in the visible range [25]. In such a configuration, the radiative transfer equation that models the transfer of the radiative intensity can be integrated along an optical pathway, such as the one followed by the collimated laser beam inside the flame in Figs. 1(a) and 1(b). When the laser is off (shutter closed), the energy $\mathcal{E}_\lambda^{(\mathrm{off})}$ accumulates on a pixel of the camera during a time Δt due to the steady impinging flux emitted by the flame at wavelength λ. When the laser is on (shutter open), the energy $\mathcal{E}_\lambda^{(\mathrm{on})}$ accumulated on the same pixel is $\mathcal{E}_\lambda^{(\mathrm{off})}$ complemented by the energy deposited by the incident noncoherent light ray. Measuring consecutively $\mathcal{E}_\lambda^{(\mathrm{on})}$ and $\mathcal{E}_\lambda^{(\mathrm{off})}$ allows the attenuation, i.e., the difference between both quantities, to be only connected to the spectral absorption coefficient field $\kappa_\lambda(r,z)$ crossed along the optical pathway leading to the pixel considered. In practice, at every height z_i imaged on a line of pixels [see Fig. 1(c)], deconvoluting the attenuation measurements integrated over the line-of-sight leads to a system of linear equations that is solved for $(\kappa_\lambda)_{ij}$ at the locations r_j along the line. As every set of equations is shown to be ill conditioned, a Tikhonov regularization is used to stabilize the deconvolution process [23]. The whole field $\kappa_\lambda(r,z)$ can then be retrieved. The soot volume fraction field $f_v(r,z)$ can also be inferred following the Mie theory and assuming that soot particles are in the Rayleigh limit as

$$f_v(r,z) = [\lambda\, \kappa_\lambda(r,z)]/[6\,\pi\, E(m)], \tag{1}$$

where $E(m)$ is a function of the complex refractive index m of soot. Following the methodology of Kashif *et al.* [23], $E(m)$ is here adjusted to 0.43 to reproduce the peak soot volume fraction measured by Santoro *et al.* [20] at HAB = 50 mm for ethylene burning in air. The level of the mean relative uncertainty within a region where the soot volume fraction exceeds 10% of its peak value is then found to be slightly lower than 5%. However, this does not incorporate the uncertainty associated with the refractive index function of soot particles reflected in the ongoing debate about this quantity.

III. NUMERICAL SIMULATION OF THE OBSERVED STABILIZATION PROCESS

In the following paragraph, the two-dimensional, axisymmetric, numerical setup, and the applied methods to reproduce the experimentally observed stabilization process are outlined. The parallelized, finite-difference code CIAO solves the Navier-Stokes equations in the low-Mach-number limit, utilizing spatial and temporal staggering, together with Crank-Nicolson type time advancement [26,27]. The Poisson equation for pressure is solved by the multigrid HYPRE solver and the scalar equations are solved via the bounded quadratic upstream interpolation for convective kinematics (BQUICK) scheme, based on the QUICK scheme of Leonard [28]. The temperature and species equations are advanced by introducing a symmetric operator split of Strang [29] and the chemistry operator uses a time-implicit backward difference method similar to that implemented in CVODE [30]. The flow is treated as a multicomponent mixture, where diffusion is approximated by the Curtiss-Hirschfelder approach [31] together with a correction velocity to account for mass conservation. The second-order Soret diffusion caused by temperature gradients is taken into account for all species, while heating due to viscous dissipation, as well as the second-order Dufour process are neglected. The chemical mechanism [32], containing 47 species and 290 reactions, was shown to predict soot precursors, including PAH chemistry. Gas phase and soot radiation is implemented with a discrete ordinates method (DOM) [33] including CO_2, CO, and H_2O. The hybrid method of moments (HMOM) [34] predicts soot quantities by taking the volume and surface of the soot particles into account. To account for the magnetic field influence, the body force term $\mathbf{F}_i$ acting on a chemical species i and its resulting drift are added to the momentum, species, and temperature equations [35]. The force can be expressed as

$$\mathbf{F}_i = \frac{1}{2\,\mu_0}\rho\, Y_i\, \chi_i\, \nabla(\mathbf{B}^2), \tag{2}$$

where $\mu_0 = 4\pi \times 10^{-7}$ is the magnetic permeability of vacuum, Y_i the mass fraction of species i, and χ_i its magnetic susceptibility per unit mass. The latter quantity is given by Curie's law as

$$\chi_i = \frac{N_A\, g_L^2\, \mu_B^2\, S_i(S_i+1)\,\mu_0}{3\,k\,T\,m_i}, \tag{3}$$

where $N_A = 6.022 \times 10^{23}$ 1/mol, $g_L = 2$ and $\mu_B = 9.274 \times 10^{-24}$ J/T are the Avogadro number, the Lande's g-factor, and the Bohr magneton, respectively. $k = 1.38 \times 10^{-23}$ J/K is the Boltzmann constant, T the temperature, and m_i the molar mass of species i. The total angular momentum of the species i electron spin is defined as S_i. The Lorentz force on ionic species is assumed negligible, due to the absence of ionizable substances like alkali elements [36]. The numerical setup corresponds to the experimental configuration. The burner nozzle extends 14 mm into the computational domain and the coflow duct's exit plane is located 11 mm into the domain. In the following the origin is set to the intersection of the vertical burner axis of symmetry and the fuel nozzle's exit plane. By choosing a numerical domain of 300 mm in the radial and 120 mm in the axial directions, it is ensured that the results are not affected by the numerical domain boundaries. At the bottom boundary, inflow conditions are used for the fuel and oxidizer flows, surrounded by stagnating air. Symmetry conditions are applied on the centerline, free-slip on the free-stream side, and zero gradient conditions on the top boundary. The mesh is nonuniform, and cylindrical with 192 (z)× 240 (r) control volumes. The minimum resolution is 0.02 mm in both the axial and radial directions close to the nozzle outlet and in regions of high-temperature and soot-volume-fraction gradients. The inflow temperature and pressure are set to 298 K and 1 atm, respectively. The oscillating non-premixed flame simulation is initialized from the steady solution and evaluated after 10 cycles, corresponding to 0.64 s in real time. The number of cycles needed to ensure a fully periodic state was identified by a start-up transient analysis [37]. The here-employed numerical methods and soot formation models have been validated in an earlier paper [27] by comparing a steady ethylene flame

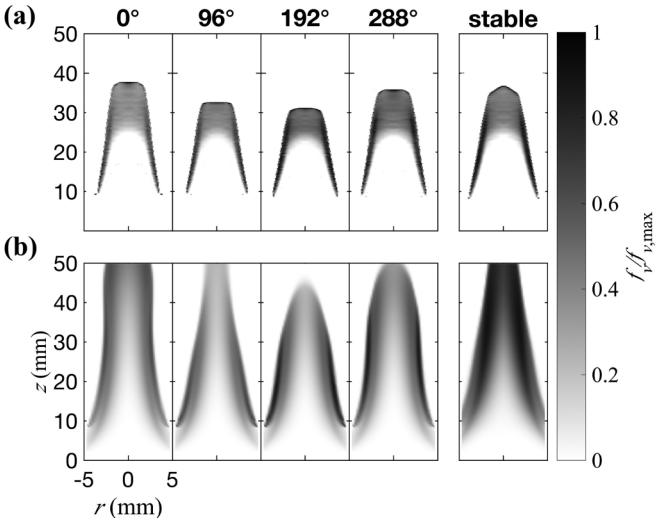

FIG. 2. Normalized soot volume fraction fields $f_v/f_{v,max}$. Experiments (a) and simulations (b). The leftmost four images show oscillating fields without magnetic field, the isolated image on the right shows the steady flame stabilized by a magnetic field. The phase angle is computed as $\phi = 360^\circ f\,\Delta t$, where f is the respective frequency (experiment: 12.6 Hz; simulation: 15.6 Hz) and Δt the physical time after the occurrence of the maximum flame height.

burning in a coflow stream of air to color-ratio pyrometry and laser-induced incandescence measurements from two different laboratories. The soot formation and oxidation zones have been well predicted as well as the location and the magnitude of the peak soot volume fraction. The impact of flame oscillations on the soot predictions was investigated in the same paper [27] by pulsing the described steady coflow flame at two frequencies. Again, the trends were well predicted. As observed in the experiments, the computed flames were oscillating at the prescribed pulsing frequencies and the instantaneous peak soot volume fraction was shown to shift from the centerline to the wing of the flame within one oscillation cycle. Also, the expulsion of the soot pocket and the subsequent flame collapse occurred in temporal agreement with the measurements. Here, the oscillation frequency is not induced by an external flow pulsing but by buoyancy and therefore it depends on other flame parameters, such as the local flame temperature. Still, the computed and measured oscillation frequencies are very close at 15.6 Hz and 12.6 Hz, respectively. Furthermore, as in Ref. [27], the changes of the peak soot volume fraction in the wings of the oscillating flame can be reproduced numerically. Figure 2 displays in the left-most four images the measured [Fig. 2(a)] and computed [Fig. 2(b)] soot volume fraction fields for one oscillation cycle without magnetic field. The local soot volume fraction is normalized by the peak soot volume fraction $f_{v,max}$ of 17 ppm and 63 ppm in the experiments and the numerical simulations, respectively. The peak soot volume fraction and hence the axial extension of the soot volume fraction field are overpredicted in the simulation. However, comparing the present simulations with state-of-the-art simulations [38] of soot production in non-premixed flames, the agreement between experiments and numerical simulations can be considered good. Finally, and most importantly, with the original experimental observation we are focusing on in this paper, a magnetic flame instability mitigation could be reproduced computationally. In both the experiments and the simulation, the non-premixed flame is stabilized with a $\nabla(\mathbf{B}^2)$ magnitude of 18.2 T^2/m. Based on the simulations' capability of reproducing the experimentally observed natural flame oscillation as well as the discovered flame stabilization with applied magnetic gradient, we are confident that the simulations reproduce the experimental results within the required scope to use the numerical simulation to function as the base result for the stability analysis performed later in this paper.

IV. MECHANISMS DRIVING THE NON-PREMIXED FLAME STABILIZATION

After showing that the experimentally observed instability suppression could be reproduced numerically, the potential mechanisms that drive the phenomenon are now assessed. Figure 3 shows the normalized radial profiles for the axial velocity (a), temperature (b), and ethylene (c) and oxygen (d) mass fractions for three nondimensional heights above the burner z/D_f. The profiles are obtained by the corresponding dimensional variables from the two-dimensional numerical

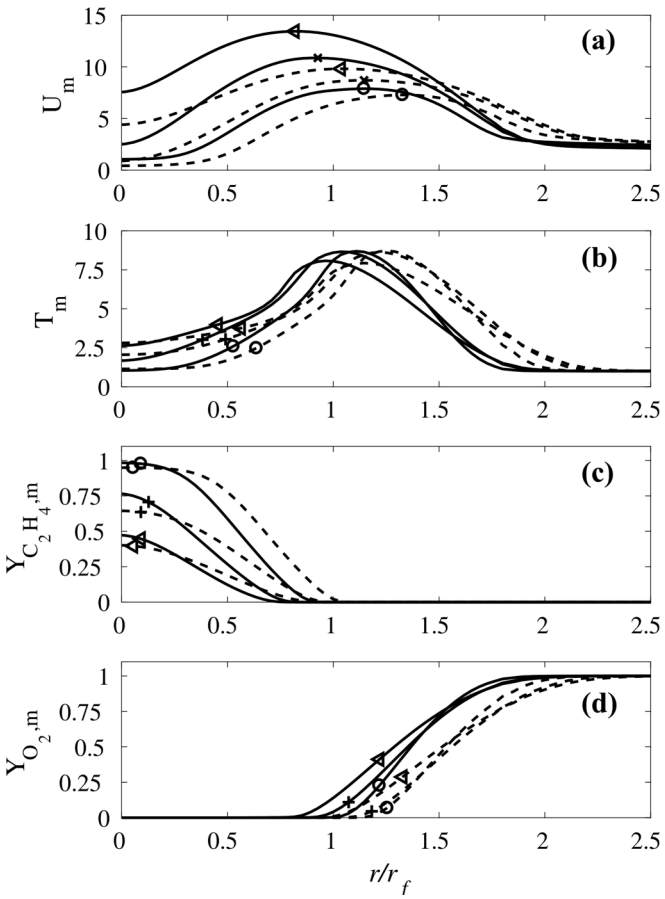

FIG. 3. Normalized computed radial mean flow profiles. (a) Axial velocity U_m, (b) temperature T_m, and (c) ethylene $Y_{C_2H_4,m}$ and (d) oxygen $Y_{O_2,m}$ mass fractions at $z/D_f = 0.4$ (circle), 0.6 (cross), and 1.0 (triangle) without (solid line) and with (dashed line) exposure to the steady magnetic-field gradient.

simulation. The variables are time averaged over one cycle (64 ms) with a discrete data set sampled every millisecond. Then, the radial distance, the axial velocity, the temperature, and ethylene and oxygen mass fractions are nondimensionalized with respect to the fuel nozzle inner radius $r_f = 5.5$ mm, the fuel inflow mean velocity $U_{f,\text{in}} = 0.063$ m/s, the inlet temperature $T_{\text{in}} = 298$ K, the unity ethylene mass fraction at the inflow, and the coflow mixture's oxygen mass fraction of 0.47, respectively. Three nondimensional heights above the burner $z/D_f = 0.4$, 0.6, and 1.0 are displayed for both magnetic field cases. For both conditions, the peak velocity increases with increasing z/D_f due to the buoyant acceleration of the hot combustion gases. The observed changes in the nondimensional mean flow profiles are consistent with the findings by Jocher *et al.* [39]. Among the species present in the combustion process, the major contribution to the magnetic force is attributed to the paramagnetic oxygen molecules at ambient conditions in the coflow, due to their high mass fraction at comparably low temperatures [35]. The resulting magnetic force per unit volume $\mathbf{f}_{\text{mag}}$ that initiates and sustains the so-called thermomagneto convection can then be expressed as [39]

$$\mathbf{f}_{\text{mag}} = \left[\rho\, Y_{O_2}\, \chi_{O_2} - \rho^{(\infty)} Y_{O_2}^{(\infty)} \chi_{O_2}^{(\infty)}\right] \frac{\nabla(\mathbf{B}^2)}{2\,\mu_0}. \tag{4}$$

The superscript (∞) indicates here the conditions away from the flame. As shown by Jocher *et al.* [39], the term between brackets in Eq. (4) is always negative for non-premixed flames. As a result, a significant thermomagneto convection can be sustained and is here opposed to buoyancy due the upward direction of $\nabla(\mathbf{B}^2)$. The global residence time inside the flame is then increased when increasing the magnitude of the upward $\nabla(\mathbf{B}^2)$ leading to enhanced soot production. Consequently, the thermal expansion is also enhanced when moving from MagF0 to MagF1, leading to the outward shift of the velocity, temperature, and mass fraction profiles. The reduced peak velocity combined with the radially outward shift at MagF1 leads to a reduced peak shear layer as well as shear layer broadening (not shown here), therefore, to a possible suppression of the KH instability. Jocher *et al.* [14] argued that due to the partial compensation of buoyancy by thermomagneto convection, the particle residence time in the flame is increased, leading to a higher peak of the radially integrated soot volume fraction. Katta *et al.* [13] found that the level of soot radiation that is enhanced due to such an increase can induce a significant local flame cooling. Therefore, the buoyant acceleration of hot combustion gases is weakened and the flickering flame stabilized. Combining both findings points to the conclusion that due to the enhanced soot formation and subsequent radiation, the flame temperature decreases and therefore reduces the acceleration of hot combustion gases due to buoyancy. Consequently, the shear layer between the hot combustion gases and the cold coflow is reduced, together with the flame's sensitivity to the KH instability. The latter finding could explain why the KH instability was suppressed by the magnetic gradient in a sooting non-premixed ethylene flame, while no such stabilization could be observed for a low sooting non-premixed methane flame at similar fluid dynamic conditions.

V. LOCAL STABILITY ANALYSIS

Finally, the growth rates of small perturbations in the non-premixed flame at MagF0 and MagF1 are investigated by a spatial, local, inviscid stability analysis in cylindrical coordinates, assuming a low Mach number and a parallel and swirl-free mean flow in axial direction. The main goal is to show that this basic theory can qualitatively predict the influence of the magnetic gradient on the spatial growth rates of small perturbations in the flame. When discussing the perturbation's growth rate $-\alpha_i$ obtained by a local spatial stability analysis, it is important to keep in mind that it describes the instability behavior of the local mean flow but not of the entire flow field. Still, it provides a framework to identify the external excitation frequency β that could be necessary to control the flow [40].

An inviscid analysis is performed and justified here based on the findings of Mahalingam *et al.* [41] that $-\alpha_i$ at a finite Reynolds number is usually lower than in the inviscid case. The governing equations for continuity and momentum [42] are complemented by equations for temperature and fuel and oxidizer mass fractions. For the chemical source term, a one-step reaction model is implemented as described by Mahalingam *et al.* [41]. The influence of the magnetic body force implementation into the governing equations used for the stability analysis was found to be negligible compared with the changes in the computed mean flow profiles. For the same reason, the gravitational force is not considered in the governing equations of the stability analysis [1]. Therefore, magnetic field and buoyancy influences actually impact the stability analysis results only through the mean flow obtained from the two-dimensional simulation, where both effects are considered. The normalized mean flow profiles for the axial velocity U_m, the temperature T_m, and the ethylene $Y_{C_2H_4}$ and oxygen Y_{O_2} mass fractions shown in Fig. 3 are used as input profiles for the stability analysis. Additional input parameters are the molecular weights of ethylene and the oxidizer. The stoichiometric coefficients applied here are 1 and 3, respectively. Similarly to Mahalingam *et al.* [41] the nondimensional value of the activation energy is kept equal to 3, the heat release parameter to 1000, and the Damköhler number to 8 for all cases shown here. The Lewis and Prandtl numbers are assumed unity and the Reynolds number infinity [41]. In addition, the Soret and Dufour effects, diffusion due to pressure gradients, and the effects of radiation are not considered in the perturbation equations. Due to the low Mach assumption, the constant thermodynamic pressure appears in the thermal equation of state, hence, ρ_{m} is directly proportional to $1/T_m$. In the following, only axisymmetric perturbations ($m = 0$) are considered. The perturbations are assumed three dimensional, while the mean flow is one dimensional in the streamwise direction.

The resulting growth rates $-\alpha_i$ of this generalized eigenvalue problem of β range are shown in Fig. 4 for the mean flow profiles in Fig. 3. For every height z/D_f studied, the peak $-\alpha_i$ is higher for MagF0 as compared to that for MagF1. This suggests that the flow is more prone to develop an instability without the magnetic gradient exposure. Furthermore, the neutral stability point at which $-\alpha_i$ approaches zero is always found at lower β for MagF1. Thus, the magnetic gradient

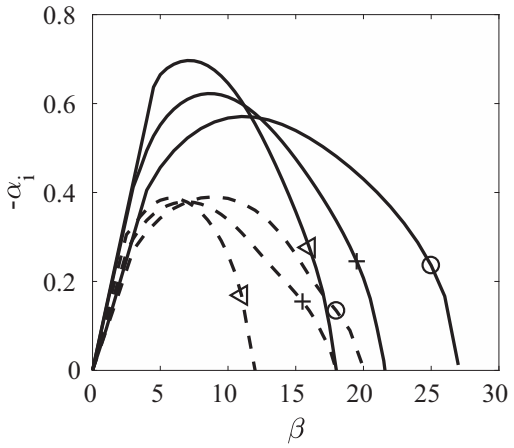

FIG. 4. Perturbation growth rate $-\alpha_i$ as a function of the perturbation frequency β. Without (solid line) and with magnetic field influence (dashed line) for $z/D_f = 0.4$ (circle), 0.6 (cross), and 1.0 (triangle).

exposure reduces the unstable frequency range. Although, according to the experiment, the growth rate for MagF1 should be negative over the whole range of frequencies, it is worth reminding that the conducted analysis addresses local stability and that a viscous stability analysis will show lower amplification rates [41]. For a more quantitative agreement, extensive efforts should be devoted to the development of a global stability analysis. Still, the basic theoretical tool that we contributed here to extend unveils a stabilizing tendency supporting the experimental observations.

VI. CONCLUSIONS

We conclude that the exposure to an upward gradient of the square of the magnetic flux density can reduce a non-premixed flame's sensitivity to KH instabilities by increasing the soot content and soot expulsion to the environment due to flame quenching in such an oscillating non-premixed flame can then be inhibited. Furthermore, we show that the flow modification by a magnetic gradient severely changes the non-premixed flame base structure and consequently soot production in the flame. Reduced growth rates for perturbations in a non-premixed flame under a magnetic gradient exposure could be identified by a local stability analysis. We anticipate our investigation to be a starting point for more sophisticated combustion control techniques. In future investigations the steady non-premixed sooting flame will be submitted to a downward gradient of the square of the magnetic flux density to assess a possible soot formation reduction induced by the resulting magnetic body force and the gravitational force pointing into the same direction. Another potential implementation could be the systematic shaping of magnetic fields [43,44] to achieve a well defined modification of combustion processes.

ACKNOWLEDGMENTS

This work was performed using HPC resources from GENCI-CINES (Grant No. 2015-c20152b7144). It was financially supported by the Université franco-allemande/Deutsch-Französische Hochschule. The authors are grateful to M. Kashif, H. Dutilleul, and J. M. Citerne for their technical support and to Lutz Lesshafft for providing the base code for the stability analysis and his valuable comments. The optical setup was partly funded with the support of the Centre National d'Etudes Spatiales (CNES) under Contract No. 130615.

[1] J. Buckmaster and N. Peters, Symp. (Int.) Combust. **21**, 1829 (1988).
[2] C. R. Ghezzi, E. M. de Gouveia Dal Pino, and J. E. Horvath, Astrophys. J. **548**, L193 (2001).
[3] B. M. Cetegen and K. D. Kasper, Phys. Fluids **8**, 2974 (1996).
[4] M. A. Habib, H. M. Badr, S. F. Ahmed, R. Ben-Mansour, K. Mezghani, S. Imashuku, G. J. la O', Y. Shao-Horn, N. D. Mancini, A. Mitsos, P. Kirchen, and A. F. Ghoneim, Int. J. Energy Res. **35**, 741 (2010).
[5] M. P. Sierra-Vargas and L. M. Teran, Respirology **17**, 1031 (2012).
[6] P. T. O'Shaughnessy, Environ. Sci.: Processes Impacts **15**, 49 (2013).
[7] M. R. Heal, P. Kumar, and R. M. Harrison, Chem. Soc. Rev. **41**, 6606 (2012).
[8] E. P. Agency, Environmental Protection Agency—Control of Emissions from Nonroad Spark-Ignition Engines and Equipment; Final Rule (2008), https://www.federalregister.gov/documents/2008/10/08/E8-21093/control-of-emissions-from-nonroad-spark-ignition-engines-and-equipment.
[9] E. Commission, Communication from the Commission to the European Parliament, the Council, the European Economic and Social Committee and the Committee of the Regions - A Clean Air Programme for Europe (2013), http://eur-lex.europa.eu/legal-content/EN/TXT/?uri=CELEX:52013DC0918.
[10] E. P. Agency, Environmental Protection Agency—Control of Hazardous Air Pollutants from Mobile Sources; Final Rule (2007), https://www.federalregister.gov/documents/2007/02/26/E7-2667/control-of-hazardous-air-pollutants-from-mobile-sources.
[11] J. C. Hilliard and F. J. Weinberg, Nature **259**, 556 (1976).
[12] P. Johnston and J. Lawton, Nature **230**, 320 (1971).
[13] V. R. Katta, W. M. Roquemore, A. Menon, S.-Y. Lee, R. J. Santoro, and T. A. Litzinger, Proc. Combust. Inst. **32**, 1343 (2009).
[14] A. Jocher, H. Pitsch, T. Gomez, and G. Legros, Proc. Combust. Inst. **35**, 889 (2015).
[15] O. Fujita, K. Ito, T. Chida, S. Nagai, and Y. Takeshita, Symp. (Int.) Combust. **27**, 2573 (1998).
[16] R. J. Twardzik, Apparatus for subjecting hydrocarbon-based fuels to intensified magnetic fields for increasing fuel burning efficiency, US Patent No. US5558765 A (1996).
[17] A. Menzell, P. Baker, and J. Kostic, Emission control devices, US Patent No. US20070295412 A1 (2007).
[18] D. de John, Assembly and process for improving combustion emissions of a combustion apparatus, US Patent No. US7918920 B2 (2011).

[19] See Supplemental Material at http://link.aps.org/supplemental/10.1103/PhysRevE.95.063113 for the experimental evidence of the magnetically induced flame stabilization and re-oscillation.
[20] R. Santoro, H. Semerjian, and R. Dobbins, Combust. Flame **51**, 203 (1983).
[21] G. Blanquart, P. Pepiot-Desjardins, and H. Pitsch, Combust. Flame **156**, 588 (2009).
[22] G. Blanquart and H. Pitsch, Combust. Flame **156**, 1614 (2009).
[23] M. Kashif, J. Bonnety, P. Guibert, C. Morin, and G. Legros, Opt. Express **20**, 28742 (2012).
[24] G. Legros and J. Torero, Proc. Combust. Inst. **35**, 2545 (2015).
[25] F. Liu, D. Snelling, K. Thomson, and G. Smallwood, Appl. Phys. B **96**, 623 (2009).
[26] O. Desjardins, G. Blanquart, G. Balarac, and H. Pitsch, J. Comput. Phys. **227**, 7125 (2008).
[27] A. Jocher, K. Foo, Z. Sun, B. Dally, H. Pitsch, Z. Alwahabi, and G. Nathan, Proc. Combust. Inst. **36**, 781 (2017).
[28] B. Leonard, Comput. Methods Appl. Mech. Eng. **19**, 59 (1979).
[29] G. Strang, SIAM J. Numer. Anal. **5**, 506 (1968).
[30] P. N. Brown, G. D. Byrne, and A. C. Hindmarsh, SIAM J. Sci. Stat. Comput. **10**, 1038 (1989).
[31] T. P. Coffee and J. M. Heimerl, Combust. Flame **43**, 273 (1981).
[32] F. Bisetti, G. Blanquart, M. E. Mueller, and H. Pitsch, Combust. Flame **159**, 317 (2012).
[33] F. Liu, H. Guo, and G. J. Smallwood, Combust. Flame **138**, 136 (2004).
[34] M. E. Mueller, G. Blanquart, and H. Pitsch, Proc. Combust. Inst. **32**, 785 (2009).
[35] E. Yamada, M. Shinoda, H. Yamashita, and K. Kitagawa, Combust. Flame **135**, 365 (2003).
[36] G. Legros, T. Gomez, M. Fessard, T. Gouache, T. Ader, P. Guibert, P. Sagaut, and J. Torero, Proc. Combust. Inst. **33**, 1095 (2011).
[37] S. Dworkin, B. Connelly, A. Schaffer, B. Bennett, M. Long, M. Smooke, M. Puccio, B. McAndrews, and J. Miller, Proc. Combust. Inst. **31**, 971 (2007).
[38] A. Veshkini, N. A. Eaves, S. B. Dworkin, and M. J. Thomson, Combust. Flame **167**, 335 (2016).
[39] A. Jocher, J. Bonnety, H. Pitsch, T. Gomez, and G. Legros, Proc. Combust. Inst. **36**, 1377 (2017).
[40] P. Huerre and P. A. Monkewitz, Annu. Rev. Fluid Mech. **22**, 473 (1990).
[41] S. Mahalingam, B. J. Cantwell, and J. H. Ferziger, Report No. TF-43 (1989).
[42] L. Lesshafft and P. Huerre, Phys. Fluids **19**, 024102 (2007).
[43] J. E. Martin and A. Snezhko, Rep. Prog. Phys. **76**, 126601 (2013).
[44] K. J. Solis and J. E. Martin, Soft Matter **10**, 9136 (2014).